Journal of Mining and Environment (JME) Vol. 17, No. 5, 2026, 1581-1603

Shahrood University of Technology

Journal of Mining and Environment (JME)

Journal homepage: www.jme.shahroodut.ac.ir

Iranian Society of Mining Engineering (IRSME)

Integration between Downhole Thermoelectric Power Generation and SiC-Based Inverter in an Innovative Design to Operate the ESP Pump Without a Cable

Mohamed Yehia Amer[1]*, Said Kamel Salem[2], and Ibrahim Salahudin Mohamed[2]

1. Egyptian Drilling Company (EDC), Egypt.
2. Faculty of Petroleum and Mining Engineering, Suez University, Egypt

Article Info

Received 23 February 2026
Received in Revised form 14 June 2026
Accepted 21 August 2026
Published online 21 August 2026

DOI: 10.22044/jme.2026.17537.3488

Keywords

Oilfield geothermal resource wells
Thermoelectric technology
ESP pump electrical inverter
ESP without cable

Abstract

Electric submersible pumps (ESPs) are among the most widely deployed artificial lift systems in the petroleum industry; however, their operation depends heavily on surface-supplied electrical power transmitted through long downhole cables, resulting in significant energy losses, high installation costs, reliability challenges, and increased carbon intensity. Simultaneously, large quantities of geothermal energy remain unused within deep hydrocarbon wells despite the substantial thermal gradients naturally available along the wellbore. This study introduces a novel multidisciplinary framework that transforms the well itself into an integrated energy-generation system by coupling geothermal heat recovery, thermoelectric power generation, advanced power electronics, and ESP technology. Unlike conventional approaches that treat geothermal energy and artificial lift as separate domains, the proposed concept establishes a unified architecture that converts otherwise wasted thermal energy into usable electrical power for ESP operation, creating a new pathway toward energy-autonomous and cable-reduced artificial lift systems. The proposed framework combines a two-dimensional wellbore heat-transfer model, thermoelectric energy conversion, and silicon-carbide-based power conditioning with a complete ESP design methodology including inflow performance analysis, total dynamic head determination, pump selection, and stage optimization. A case study on Well AG-119X in Abu El Gharadig Field, Western Desert, Egypt, with a pump setting depth of 19,000 ft., demonstrates the technical feasibility of hydrocarbon–geothermal co-production and predicts a thermoelectric generation potential of approximately 350 kW under optimized conditions. Beyond demonstrating energy recovery, the study establishes a scalable roadmap for integrating geothermal resources directly into artificial lift infrastructure, reducing dependence on external power supply, improving overall system efficiency, and enabling more sustainable oil production. The proposed approach represents a step toward the convergence of petroleum engineering, geothermal energy, thermoelectric science, and power electronics, providing a foundation for next-generation self-powered ESP systems.

1. Introduction

Over the past decade, unconventional oil and gas development has significantly altered global energy dynamics, particularly in the United States and the Middle East. However, extracting hydrocarbons from low-permeability reservoirs demands capital-intensive drilling and multistage hydraulic fracturing. Operators face severe output decline rates coupled with high water production, creating major economic, technical, and environmental liabilities regarding produced water management [1,2].

To broaden geothermal power generation approaches and increase the number of eligible oil wells, thermoelectric technology has been introduced into geothermal applications[3].This technology

Corresponding author: mohammed.haam@pme.suezuni.edu.eg (M.Y. Amer)

operates based on the Seebeck effect, whereby thermoelectric modules directly convert heat into electrical energy under a temperature gradient[4,5]as shown in (Figure 1) without the need for mechanical components such as turbines. Previous studies have modeled, optimized, and experimentally validated thermoelectric systems for geothermal power generation[6,7].

$$V = \alpha(TH - TC) \quad (1)$$

Where are:
TH - the hot side
TC - the cold side
α - Seebeck coefficient

In general, the efficiency of thermoelectric power generation largely depends on the dimensionless figure of merit, zT[9], as shown in (Figure 2) which is an intrinsic property of thermoelectric materials used to evaluate their performance. A higher zT value indicates a stronger capability to convert thermal energy into electrical power efficiently[10]. Experimental investigations and economic assessments have also been conducted to evaluate the feasibility of geothermal electricity generation using a thermoelectric generator.

$$zT = \frac{\alpha^2 T}{k\sigma} = \frac{\alpha^2 (TH - TC)}{2k\sigma} \quad (2)$$

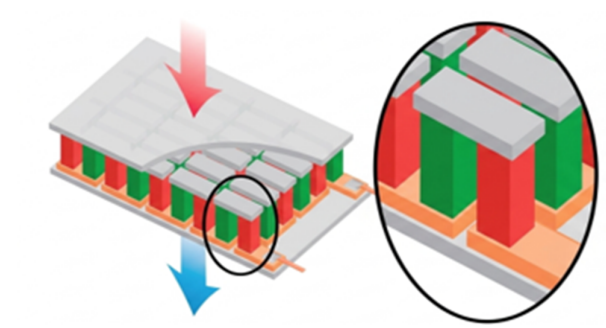

Figure 1. Schematic of a typical thermoelectric generator[8]

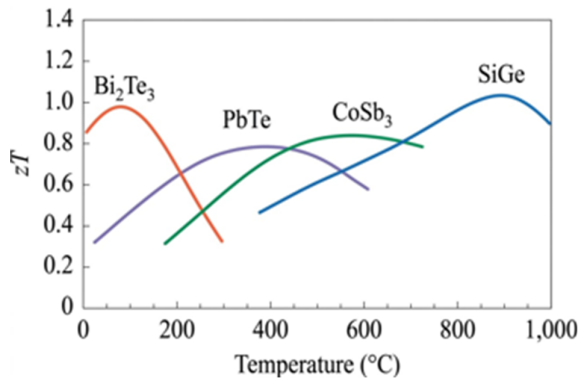

Figure 2. ZT values of different materials in given temperature ranges[9]

1.1. Downhole geothermal power generation in oil wells

A recently proposed downhole geothermal power generation configuration (Figure 3) maximizes the temperature gradient across production-tubing-mounted Thermoelectric Generators (TEGs) by using small-diameter pipes in the casing-tubing annulus to inject cold water[9]. This setup establishes the necessary temperature difference for electrical power generation between the hot produced fluids on one side of the TEG and the cold injected water on the opposite side[11].

Vertical wells completed via the plug-and-perforation method can be retrofitted to harvest subsurface geothermal energy by attaching Thermoelectric Generators (TEGs) [12]. to the exterior of the tubing[14,13]. Circulating cold water inside the tubing creates a low-temperature interface, while hot produced fluids flowing through the annular space supply a high-temperature boundary.as shown in (Figure 4) Because the extended vertical section of the wellbore stays exposed to peak formation temperatures, this arrangement sustains a high thermal gradient across the TEGs[15]. to maximize continuous electrical power generation.[16,17].

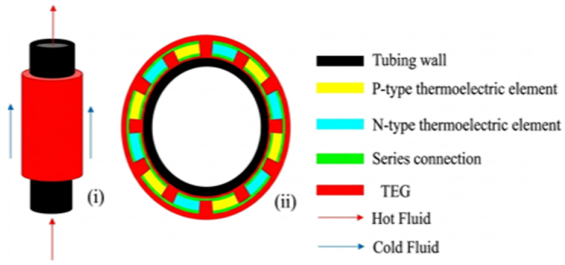

Figure 3. Schematics of TEG installation on the tubing[9]

As illustrated in (Figure 5), vertical wells experience temperature gradients along the wellbore[18] that impact the thermal differential across TEGs and influence total power generation. However, the vertical configuration offers significant operational flexibility: suspending the tubing and attached TEGs from the wellhead allows for easy retrieval and reinstallation[19], while TEG placement can be tailored for each stage based on local flow rates to optimize electrical output[20].

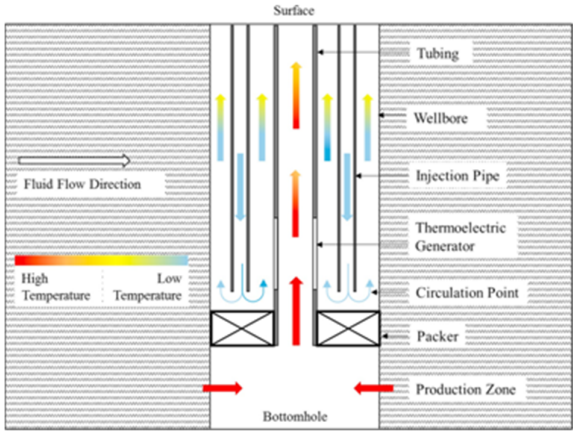

Figure 4. Schematic of downhole power generation in a waterflooding well[15]

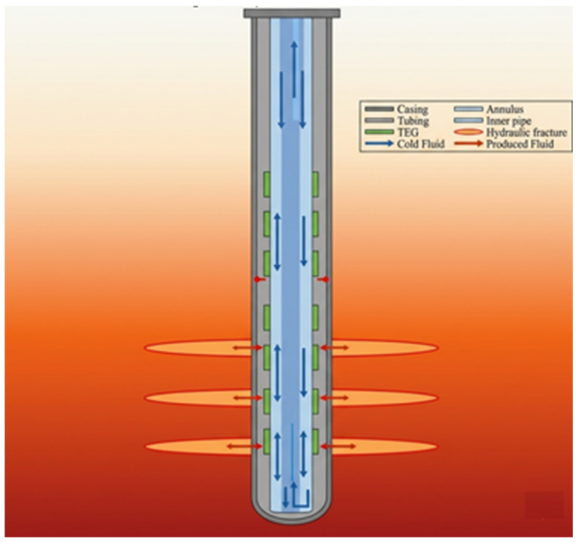

Figure 5. Schematics of downhole power generation in unconventional vertical wells

Driven by population growth, rapid industrialization, and the depletion of fossil fuels, the intensifying global energy crisis has brought geothermal energy into focus as an abundant, widely available, and cost-effective renewable resource[21]. However, major technical barriers, primarily low energy conversion efficiency and the underutilization of thermal potential, continue to hinder its large-scale commercial deployment [22,23].

TEGs have been particularly well studied for surface-based geothermal power generation. For example, Sasaki conducted a long-term field test at the Naruko Onsen hot spring in Japan,[24,25,26]. where the system operated for nearly 9,000 hours over 1.5 years, producing a total of 1,927 kWh[27]. with a maximum output of 889 W[28]. Ahiska and Mamur developed a power analysis framework for geothermal thermoelectric generators using water as the working fluid. Similarly, Catalan and coauthors designed and experimentally evaluated a prototype system employing a water-ammonia mixture within a circulating thermal siphon for Enhanced Geothermal System applications[29].

Recent research demonstrates that modular [30,31,32]Thermoelectric Generators (TEGs), whether deployed in direct field tests,[8,33] built as high-capacity modules, or integrated into hybrid power systems, significantly expand geothermal energy conversion across various operational scales[34,35].

Several researchers have also explored hybrid downhole systems that integrate TEGs with other energy conversion technologies.[36,37,38] Xie et al. proposed a downhole in-situ power generation system combining TEGs with a magnetic levitation generator within a large-scale heat pipe, achieving promising efficiency in experimental evaluations.[39] Lou et al. investigated a hybrid ORC–TEG system by incorporating a TEG layer into a coaxial geothermal well[40,41,42],Overall, existing research has demonstrated the technical viability of TEGs for geothermal power generation. While extensive numerical and experimental studies have been conducted on surface-based TEG systems,[43,44,45].

1.2. Electric Submersible Pump (ESP)

Unlike most artificial lift techniques, such as gas lift or sucker-rod pumping, whose origins cannot be traced to a specific individual or time period [46,47,48] electrical submersible pumping (ESP) has a clearly documented inventor. ESP technology was conceived and developed in the late 1910s by the Russian engineer Armais Arutunoff. In 1911, [49,50,51]Arutunoff founded the Russian Electrical Dynamo of Arutunoff, commonly known as REDA[52,53,54.].

1.3. Electrical Inverter

Due to their high efficiency and torque density, synchronous reluctance motor (SynRM) drive systems are gaining significant attention. As conventional silicon (Si) semiconductor devices approach their physical performance limits [55], wide-bandgap (WBG) devices are being extensively researched to achieve higher power density, focusing on VSI switching behavior [56], switching modeling [57], loss estimation [58], and trajectory optimization [59,60].

Silicon carbide (SiC) power devices including SiC-IGBTs and SiC MOSFETs [61,62]consistently outperform conventional silicon (Si) devices across diverse applications,[63,64,65] such as motor drives,

inverters, and high-voltage energy conversion systems up to 10 kV[66,67,68]. Studies demonstrate that SiC technology achieves higher overall efficiency and superior high-temperature performance due to faster switching speeds, lower on-state resistance, and significantly reduced switching losses.[69].

Table 1. Summary of Previous Studies and Research Gap

Reference	Downhole TEG	Heat Transfer Model	Power Electronics	ESP Integration	Limitation
Wang et al. (2018)	✓	✓	✗	✗	Focused on generation only
Wang et al. (2019)	✓	✓	✗	✗	No artificial lift application
Chen et al.	✓	✗	✗	✗	Material optimization only
Zare et al.	✓	✗	✗	✗	Surface geothermal application
Present Study	✓	✓	✓	✓	Integrated framework

Methods for calculating the peak rms current ripple in DC-link capacitors are presented in references[70,71,72], indicating that ripple current depends on the modulation index and phase displacement. The influence of dead time on input current ripple in three-phase VSIs is analyzed in reference [73], while a reference introduces rms input.

The effect of load imbalance on capacitor voltage ripple is verified in references [74,75,76]. A voltage-control-based theoretical approach for estimating the DC-link voltage ripple is proposed in reference [77], and reference [78] examines ripple behavior under nonlinear load currents. However, these studies do not account for the influence of variations in power factor and modulation index on peak rms voltage ripple, which is later addressed in reference [79].

1.4. Novelty and Research Gap

Significant research has been conducted on downhole thermoelectric power generation in oil and gas wells; existing studies have primarily focused on thermal modeling, thermoelectric efficiency optimization, and estimation of electrical power generation potential. The generated power was generally considered as an isolated output without investigating its direct utilization in artificial lift.

The present study addresses this gap by proposing an integrated energy-autonomous ESP architecture in which geothermal energy recovered through downhole thermoelectric generators is directly converted into usable electrical power for ESP operation through a SiC-based power

Unlike previous studies that investigated geothermal power generation as a standalone process, as shown in Table 1. The proposed framework evaluates the feasibility of transforming the oil well into a combined hydrocarbon production and electrical power generation system capable of partially or fully supporting ESP operation.

While previous research focused primarily on standalone thermoelectric power potential, thermal modeling, and material optimization, it largely neglected integration with artificial lift systems. This study addresses that gap by establishing a unified framework that combines downhole thermoelectric generation, SiC-based power conditioning, and ESP system design for integrated hydrocarbon–geothermal energy recovery.

To improve transparency and reproducibility, the major assumptions adopted in the integrated thermoelectric generation, power conditioning, and ESP design models are summarized in Table 3. These assumptions were selected based on published literature, industrial practice, and the operating conditions of the investigated well.

2 Methodology

2.1. Mathematical Model of Wellbore Temperature Distribution

2.1.1. Assumptions

To develop a mathematical model that describes heat transfer and fluid flow in vertical wells, the following Assumptions are adopted.

1. The wellbore is represented by a cylindrical geometry, and fluid inflow from the reservoir is modeled as linear flow.

2. The geothermal gradient is assumed to be constant, resulting in a formation temperature that varies linearly with depth.

3. The temperature of the fluid entering the wellbore is considered constant and equal to the reservoir's geothermal temperature, with the Joule–Thomson effect neglected.

4. Both the produced and injected fluids are treated as incompressible Newtonian fluids.

Table 2. Description of the divided subdomains

Region	Radial ranges	Physical meaning
1	• <r < r1	Inner of Inner pipe
2	r1 <r < r2	Inner pipe wall
3	r2 <r < r3	Annulus between inner pipe and tubing
4	r3 <r < r4	Tubing wall
5	r4 <r < r5	Annulus between tubing and casing
6	r5< r < r6	Casing wall
7	r6< r < r7	Cement sheath
8	r7 <r < r8	Formation

2.1.2. Geometry Schematics

The complete geometry is discretized into two-dimensional grid blocks along both the well trajectory and the radial direction, as illustrated in. (Figure 6). The domain is subdivided into several distinct regions, as summarized in Table 2. Each region is characterized by a dominant heat transfer mechanism. Convective heat transfer occurs within the annulus and at the interfaces with the inner pipe, tubing, and casing walls. In contrast, heat transfer through the pipe walls, thermoelectric generator (TEG), cement sheath, and surrounding formation is governed primarily by conductive processes[81].

2.1.3. Governing equations

Based on these assumptions, the mathematical framework is formulated in a two-dimensional cylindrical coordinate system. Fluid flow and heat transfer within this model are described using the governing equations for non-isothermal systems. For an infinitesimal control volume in this geometry, the energy conservation equation can be expressed as[82].

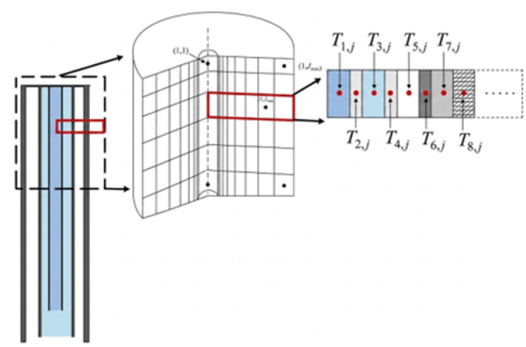

Figure 6. Simplified physical model of the vertical well with divided regions and 2-D gridlocks

$$\frac{\partial}{\partial t}\left(\frac{1}{2}\rho v^2 + \rho U\right) = -\left(\nabla \cdot \left(\frac{1}{2}\rho v^2 + \rho U\right) v\right) - \nabla \cdot q - \nabla \cdot pv - \nabla \cdot (\tau \cdot v) + \rho(v \cdot g) \quad (3)$$

Where are:

ρ the density of the fluid

v the velocity of the fluid

P stands for the pressure

U represents the internal energy of the fluid per unit mass

g is the acceleration of gravity.

The term on the left-hand side of the equation represents the rate of kinetic and internal energy change per volume, and the terms on the right-hand side represent the rate of increase of energy per volume due to convection, the rate of energy increase due to molecular transport, the rate of work done on the fluid by viscous forces,[83] rate of work done on the fluid by pressure forces, and rate of work done on the fluid by gravitational forces, respectively. The equation of mechanical energy change is

$$\frac{\partial}{\partial t}\left(\frac{1}{2}\rho v^2\right) = -\left(\nabla \cdot \frac{1}{2}\rho v^2 v\right) - \nabla \cdot pv - \nabla \cdot (\tau \cdot v) - (-\tau : \nabla v) + \rho(v \cdot g) \quad (4)$$

Subtracting Eq. (4) from (3), we can obtain the equation of change for internal energy,

$$\frac{\partial}{\partial t}(\rho U) = -(\nabla \cdot \rho U v) - \nabla \cdot q - \nabla \cdot pv - (\tau : \nabla v) \quad (5)$$

Heat conduction is modeled by using Fourier's Law, and written in cylindrical coordinates as

$$\rho C_P\left(\frac{\partial T}{\partial t}+v_r\frac{\partial T}{\partial r}+v_z\frac{\partial T}{\partial z}\right)=\frac{k_r}{r}\frac{\partial T}{\partial r}+k_r\frac{\partial^2 T}{\partial r^2}+k_z\frac{\partial^2 T}{\partial z^2} \quad (6)$$

Where are:

CP is the specific thermal capacity of the fluid,

kr is the thermal conductivity in the radial direction,

kz is the thermal conductivity in the vertical direction.

2.1.4. Initial and Boundary Conditions

After deriving the preceding equations, appropriate initial and boundary conditions are required to numerically solve the problem. It is assumed that the well has been producing for an extended period and is predominantly producing water rather than oil.[84,85] Consequently, these boundary conditions can be expressed mathematically as follows.

$$k\frac{\partial T_t}{\partial r}\bigg|_{pipewall}=h(T_{i+1}-T_i) \quad (7)$$

$$T|_{r=\infty}=T_{geothermal} \quad (8)$$

2.1.5. Effect of TEG On Temperature Distribution

The thermoelectric generators (TEGs) installed on the outer surface of the tubing can significantly modify the temperature distribution due to the thermoelectric conversion process and the Joule heat generated during this conversion[86]. To incorporate the influence of TEGs on the temperature distribution, an effective thermal conductivity parameter is introduced in the model to accurately represent the heat transfer behavior associated with thermoelectric conversion, as proposed by Baranowski et al.[87,88].

$$k_{eff}=\frac{kT_H\left(1+ZT+\sqrt{1+ZT}\right)}{2(T_H-T_C)}\left(1-\left(\frac{T_H}{T_C}\right)^{\frac{2-2\sqrt{1+ZT}}{ZT}}\right) \quad (9)$$

2.1.6. Numerical solution

$$\frac{\partial T}{\partial r}=\frac{T_{i+1,j}^{t+\Delta t}-T_{i-1,j}^{t+\Delta t}}{2\Delta r} \quad (10)$$

$$\frac{\partial T}{\partial z}=\frac{T_{i,j+1}^{t+\Delta t}-T_{i,j-1}^{t+\Delta t}}{2\Delta z} \quad (11)$$

$$\frac{\partial^2 T}{\partial r^2}=\frac{T_{i+1,j}^{t+\Delta t}-2T_{i,j}^{t+\Delta t}+T_{i-1,j}^{t+\Delta t}}{\Delta r^2} \quad (12)$$

$$\frac{\partial^2 T}{\partial z^2}=\frac{T_{i,j+1}^{t+\Delta t}-2T_{i,j}^{t+\Delta t}+T_{i,j-1}^{t+\Delta t}}{\Delta z^2} \quad (13)$$

Write the time discretization as,

$$\frac{\partial T}{\partial t}=\frac{T_{i,j}^{t+\Delta t}-T_{i,j}^{t}}{\Delta t} \quad (14)$$

And the equations in each region could be expressed as

$$A_{i,j}T_{i,j-1}^{t+\Delta t}+B_{i,j}T_{i,j}^{t+\Delta t}+C_{i,j}T_{i,j+1}^{t+\Delta t}=D_{i,j} \quad (15)$$

As a result, the temperature profile in each region can be determined by solving the governing equations together with the initial and boundary conditions using the tridiagonal matrix algorithm (Thomas algorithm). The overall heat transfer coefficient is evaluated using established methods[89] from the literature [38], based on the Nusselt number (Nu) and the hydraulic diameter (Dh), following the corresponding relationship.

$$Nu=\frac{h}{k}D_h \quad (16)$$

2.2. Mathematical Model for Inverter Design

The electrical power generated by the thermoelectric generators is produced in the form of direct current (DC), whereas the electric submersible pump (ESP) motor requires a controlled three-phase alternating current (AC) supply for reliable operation.

2.2.1. Three-Phase Two-Level Inverter

A three-phase two-level VSI is used. Whereas the inverter in the drive system consists of six Sic MOSFE as shown in (Figure 7) that the Sic MOSFET has a lower forward voltage.

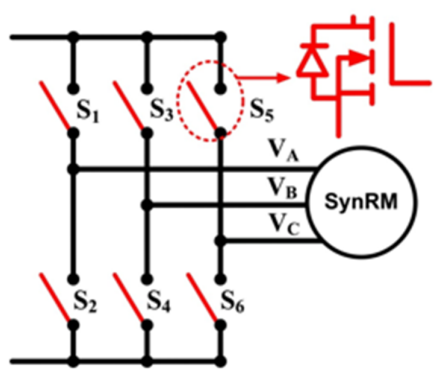

Figure 7. SiC MOSFET drive system [90]

2.2.2. SVPWM and Inverter Losses

As illustrated in (Figure 7), the three-phase inverter operates across eight valid switching states six active vectors (V1–V6) and two zero vectors (V0 [000] and V7 [111])to synthesize the reference output voltage (Figure 8a) For the zero vector, the upper switches are turned off while the lower switches are turned on. Vector duty cycles within each sector are calculated via Equation 17 using the angular position V0 (000), and modulation indices qv and mv. The overall SVPWM switching sequence is presented in Figure 8b) [91].

$$V_o^* = d_\alpha V_\alpha + d_\beta V_\beta + d_z V_z, \begin{cases} d_\alpha = \frac{T_\alpha}{T_s} = m_i * sin\left(\frac{\pi}{6} + \theta_v\right) \\ d_\beta = \frac{T_\beta}{T_s} = m_i * sin(\theta_v) \\ d_7 = d_0 = \frac{T_z}{T_s} = 1 - \left(d_\alpha + d_\beta\right) \end{cases} \quad (17)$$

Where are:

Ta, Tb, and Tz represent the time durations of vectors

Va, Vb, and the zero vector, respectively.

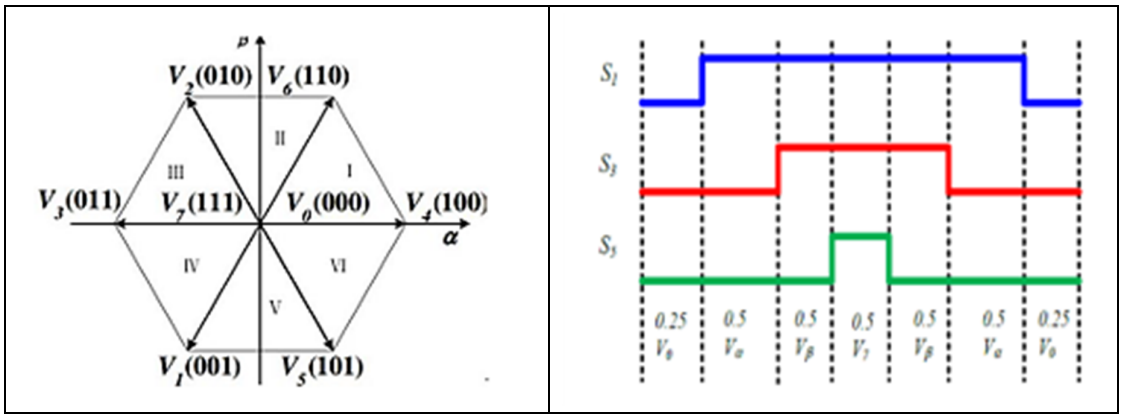

(a) (b)

Figure 8. (a) Hexagon for three-phase inverter and (b) switching sequence for continuous SVPWM for one cycle in the first sector[91]

The efficiency can be readily calculated using the evaluated output power and the total estimated losses, which comprise the machine's copper and iron losses in addition to the inverter's switching and conduction losses. In this analysis, mechanical losses are neglected.[92] Meanwhile, the copper losses of the SynRM can be easily determined from the measured winding resistance and the current amplitude. The resistance is measured at a temperature of 70 °C (resistivity = 0.0217 Ω·mm²/m). The efficiency of the drive system is expressed as follows.

$$\eta = \frac{P_o}{P_o + P_{cu} + P_{iron} + P_{inverter}} \quad (18)$$

Where are:

Po is the motor's mechanical output power,

which is determined using the FEM model's estimated torque by

$$P_o = T_e * \omega_r. \quad (19)$$

Iron losses in the SynRM are calculated using Bertotti's statistical loss theory. This theory is based on separating the total iron losses into three components: hysteresis losses, classical eddy current losses, and excess losses.

$$P_{iron} = P_h + P_c + P_e. \quad (20)$$

As shown in (Figure 9) , switching and conduction losses for an inverter switch are evaluated using its terminal voltage VS blue and current IS red [93] Averaging the instantaneous switching losses (green) and conduction losses (black) over one fundamental frequency period via Equation 21 determines the single-switch loss Ps loss based on switch and diode parameters VS, VD, IS, ID. Summing these individual losses across all switches gives the total inverter loss $P_{inverter}$[94].

$$P_{s_loss} = \frac{1}{T}\left\{\int_0^T V_S * I_S dt + \int_0^T V_D * I_D dt\right\} \quad (21)$$

2.2.3. Design of the DC-Link Capacitor

This section addresses the optimal design of the DC-link capacitor to mitigate voltage and current sags in the DC-link. The discussion begins with an analysis of the DC-link voltage ripple, followed by an examination of the analytical calculation of current ripples in the DC connection. Finally, the ideal capacitance value of the DC-link capacitor is determined[96].

2.2.3.1. Analysis of Voltage Ripple

This section examines the voltage ripple present in the DC-link of a two-level inverter. (Figure 9) illustrates the structure of a two-level three-phase inverter incorporating a DC-link capacitor and a three-phase SynRM. The three-phase motor current can be expressed as follows[97].

$$i_A = I_m cos(\omega t - \emptyset), \quad (22)$$

$$i_B = I_m cos\left(\omega t - \emptyset - \frac{2\pi}{3}\right), \quad (23)$$

$$i_C = I_m cos\left(\omega t - \emptyset + \frac{2\pi}{3}\right), \quad (24)$$

Where are I_m, w, t, and $\emptyset$ represent the peak current of the motor in A, angular frequency in rad/s, time in s, and the power factor of the motor, respectively.

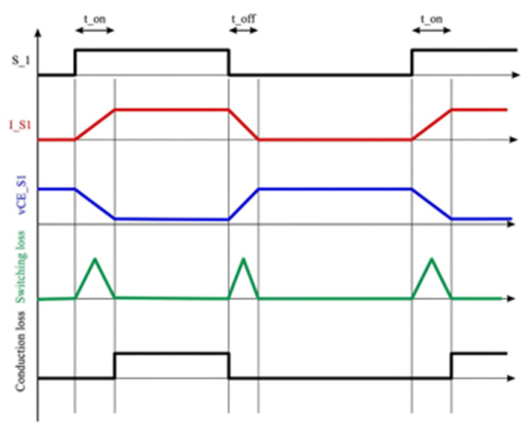

Figure 9. Calculation of switching and conduction losses[95]

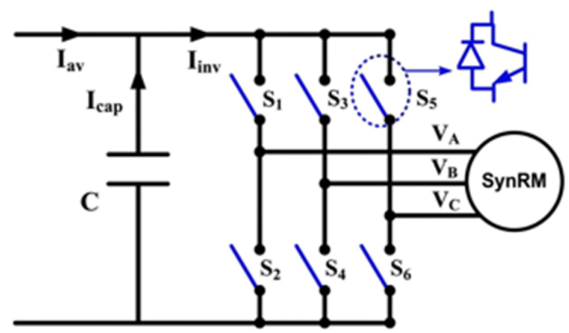

Figure 10. Two-level inverter with DC-link capacitor[98]

The analysis presented in this section is carried out based on the SVPWM scheme described in Section 3.2. Accordingly, the duty cycles of the inverter's upper switches can be expressed as follows:[99]

$$D_A\& = \frac{1}{2} + \frac{1}{2} m_i \cos\left(\omega t - \frac{\pi}{6}\right), \quad (25)$$

$$D_B\& = \frac{1}{2} - \frac{\sqrt{3}}{2} m_i \cos\left(\omega t + \frac{\pi}{3}\right) \quad (26)$$

$$D_C\& = \frac{1}{2} - \frac{1}{2} m_i \cos\left(\omega t - \frac{\pi}{6}\right) \quad (27)$$

Where are:

m_i represents the modulation index of the inverter controlled by the SPWVM.

It has a maximum value of 1, and it can be calculated by Equation 28,

V_{Line} and V_{DC} represent the peak value of the line-to-line voltage and the dc-link voltage, respectively

$$m_i = \frac{V_{Line}}{V_{DC}} \quad (28)$$

The inverter current (I_{inv}) can be calculated using the switching states of the inverter top switches and the motor currents as follows:

$$\boldsymbol{I_{inv} = S_1 i_A + S_3 i_B + S_5 i_C} \quad (29)$$

Assuming lossless inverter operation, the power in the DC-link or drawn from the battery is equal to the input power of the three-phase SynRM, as expressed in Equation 30. Consequently, the average inverter current (I_{av}) supplied by the battery can be determined using Equation 31.

$$V_{DC} I_{av} = \frac{\sqrt{3}}{2} V_{line} I_m cos\, \emptyset, \quad (30)$$

$$I_{av} = \frac{\sqrt{3}}{2} m_i I_m \cos \emptyset. \quad (31)$$

Considering the circuit shown in (Figure 10), the capacitor current (I_{cap}) can be calculated as follows:

$$I_{cap} = I_{inv} - I_{av} \quad (32)$$

The fundamental formula for the current flowing through a capacitor (icap) is defined as follows

$$i_{cap} = C \frac{dv_{cap}}{dt}. \quad (33)$$

Then the voltage ripple across the capacitor can be derived as follows

$$dv_{\text{cap}} = \Delta V = \frac{i_{\text{cap}}\, dt}{C}. \quad (34)$$

Equation 34 indicates that, for a given capacitor, the voltage ripple (ΔV) is proportional to the ampere-second value (i_{cap} dt = CΔV). By formulating an appropriate ampere-second expression, an exact equation for the minimum DC-link capacitance required to satisfy a specified voltage ripple limit can be derived. (Figure 11) presents the switching sequence along with the associated current and voltage waveforms of the upper transistors in each inverter leg. As shown in (Figure 11), no current flows through the inverter during the zero switching states (000) and (111). Owing to the symmetry observed in the voltage ripples in (Figure 11), the corresponding ampere-second equations for different switching combinations can be established [100].

$$C\Delta V_1 = -\frac{1}{2} T_s (1 - D_A) I_{av} \quad (35)$$

$$C\Delta V_2 = \frac{1}{2} T_s (D_A - D_B)(I_A - I_{av}) \quad (36)$$

$$C\Delta V_3 = \frac{1}{2} T_s (D_B - D_C)(I_A + I_B - I_c) \quad (37)$$

$$C\Delta V_4 = -\frac{1}{2} T_s D_C I_{av} \quad (38)$$

Where are:

Ts - represents the switching time ($\frac{1}{\text{Fsw}}$)

F_{sw} - is the switching frequency

The maximum ampere-second value within a given sector by considering the power factor and modulation index. The maximum ampere-second (corresponding to the peak voltage ripple, ΔVmax) can be obtained using either of the expressions C(ΔV3+ΔV4) or C ΔV4 and these expressions can be described as follows which are defined as follows:[101].

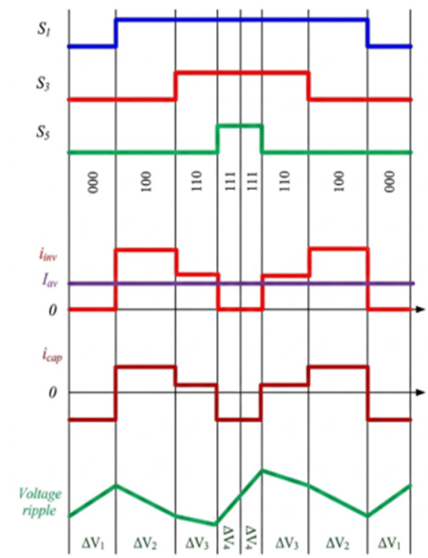

Figure 11. Top switch switching states, inverter, capacitor current and voltage [98]

$$C\Delta V_4 = -\frac{\sqrt{3}}{8} m_i I_m T_s [1 - m_i \cos(\omega t - \frac{\pi}{6})] \cos \emptyset \quad (39)$$

$$C(\Delta V_3 + \Delta V_4) = m_i I_m T_s [\frac{1}{2} \sin \omega t * \cos(\omega t - \frac{\pi}{3} - \emptyset) - \frac{\sqrt{3}}{8} \cos \emptyset * (1 - m_i \cos(\omega t - \frac{\pi}{6}) + 2 m_i \sin \omega t)]. \quad (40)$$

For sector 1, the maximum value of |CΔV4|is obtained at unity power factor (cosØ = 1), ωt = 0 or $\frac{\pi}{3}$ and the modulation index of $\frac{1}{\sqrt{3}}$. The maximum value of |CΔV4| is given by (41). To obtain the maximum value of |C(ΔV3 + ΔV4)|, a 3D plot is used, as there is no closed-form solution in terms of power factor and the modulation index. A 17.3 A peak current is used to obtain the 3D plot shown in (Figure 12).

$$|C\Delta V4|max = \frac{Im\, Ts}{16} \quad (41).$$

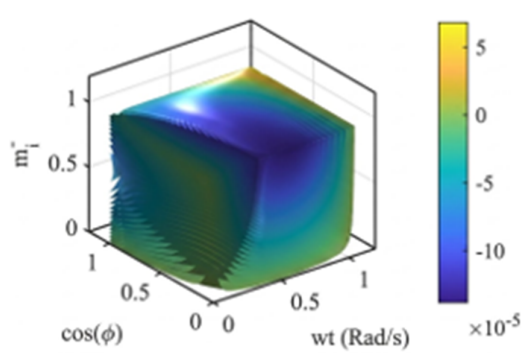

Figure 12. 3D MATLAB plot of $|C\ (\Delta V3 + \Delta V4\ )|$ at 15 kHz switching frequency and 17.3 A peak. motor current versus power factor, modulation index and ωt[76]

2.2.4. Analysis of Current Ripple

This section analyses the current ripple in the DC-link capacitor, referring to (Figure 11) for the analysis. The switching intervals $d\alpha$ and $d\beta$ associated with transitions between the (100) and (110) states are given by (1) and depicted in (Figure 13). Equations 42 and 43 provide expressions for determining the average inverter input current.[102] The average current calculated using Equation 43 is consistent with the result shown in Equation 15. In the same way, the RMS value of the inverter current can be calculated using Equations 44 and 45.

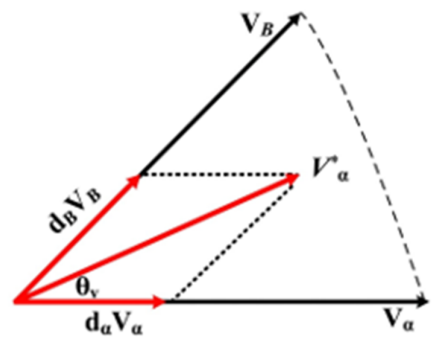

Figure 13. Reference voltage located in the first sector[76]

$$.I_{av} = d_\alpha i_A + d_\beta (i_A + i_B) = d_\alpha i_A - d_\beta i_C \tag{42}$$

$$\begin{aligned} I_{av} &= m_i cos\left(\omega t + \frac{\pi}{6}\right) * I_m cos(\omega t - \emptyset) - m_i sin(\omega t) * I_m cos\left(\omega t - \emptyset + \frac{2\pi}{3}\right) \\ &= \frac{1}{2} m_i * I_m \left\{cos(\emptyset) * \frac{\sqrt{3}}{2} - sin(\emptyset) * \frac{1}{2} - sin(\emptyset) * -\frac{1}{2} + cos(\emptyset) * \frac{\sqrt{3}}{2}\right\} \\ &= \frac{1}{2} m_i * I_m \left\{2 * cos(\emptyset) * \frac{\sqrt{3}}{2}\right\} = \frac{\sqrt{3}}{2} m_i * I_m * cos(\emptyset), \end{aligned} \tag{43}$$

$$i_{rms}^2 = d_\alpha i_A^2 + d_\beta i_C^2 \tag{44}$$

$$\begin{aligned} i_{rms}^2 &= m_i cos(\omega t + \frac{\pi}{6}) * I_m^2 cos^2(\omega t - \emptyset) + m_i sin(\omega t) * I_m^2 cos^2(\omega t - \emptyset + \frac{2\pi}{3}) \\ &= \frac{m_i * I_m^2}{2} * \{cos(\omega t - \frac{\pi}{6}) - \frac{1}{2} sin(3\omega t - 2\emptyset) + cos(\omega t - \frac{\pi}{6} - 2\emptyset)\} \\ &= \frac{m_i * I_m^2}{2\pi} * \{\frac{3}{2} + \frac{3}{2} - \frac{1}{2} cos(2\emptyset) - \frac{1}{2} cos(2\emptyset) + 3 * sin(\frac{\pi}{6} - 2\emptyset) + 3 * sin(\frac{\pi}{6} + 2\emptyset)\} \\ &= \frac{m_i * I_m^2}{2\pi} * \{1 + 4 * cos^2(\emptyset)\}. \end{aligned} \tag{45}$$

$$I_{c,rms}^2 = I_{rms}^2 - I_{av}^2 = \frac{m_i * I_m^2}{2\pi} * \{1 + 4 * cos^2(\emptyset)\} - \frac{3}{4} m_i^2 * I_m^2 * cos^2(\emptyset) \tag{46}$$

Then, the capacitor current can be calculated as follows

$$I_{c,rms} = I_m \sqrt{\frac{m_i}{2\pi} * [1 + cos^2(\emptyset) * (4 - \frac{3\pi}{2} m_i)]} \tag{47}$$

The RMS ripple dc-link current is given as follows:

$$RMS\ Ripple\ dc\text{-}link\ current = \frac{I_{c,rms}}{I_{m,rms}} = \sqrt{\frac{M}{\pi} * [1 + cos^2(\emptyset) * (4 - \frac{3\pi}{2} M)]} \tag{48}$$

Although analysis in (Figure 14) and (Figure 13b) shows peak RMS ripple current occurring at unity power factor (at modulation indices of 0.54 and 0.5, respectively)[103], Operating a three-phase SynRM at unity power factor is unrealistic. Consequently[104], calculations are based on the operating point delivering maximum output power. For the evaluated SynRM, a peak current of 17.3 A, a modulation index of 0.7244, and a power factor of 0.6176 deliver maximum power, resulting in a practical RMS ripple current of 6.5 A.

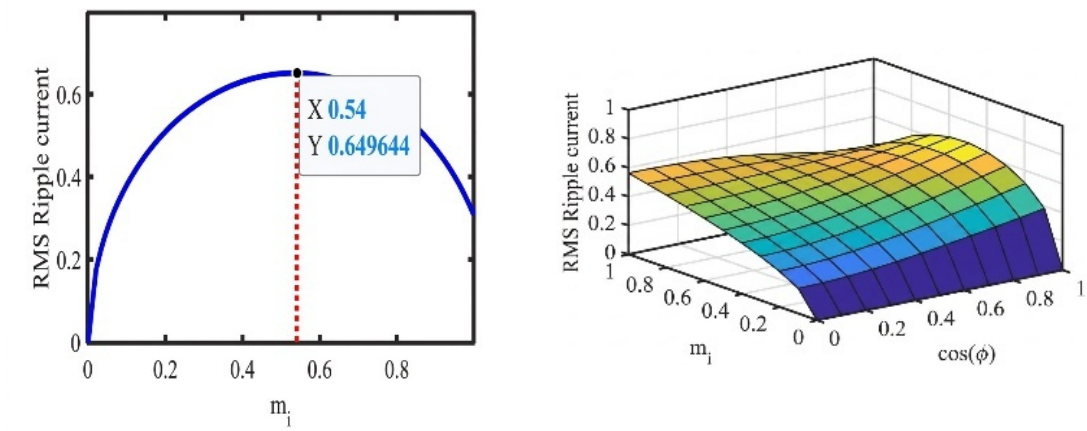

(a) (b)

Figure 14. RMS ripple current at (a) versus modulation index and at unity power factor and (b) versus modulation index and power factor[76]

2.3. Electric Submersible Pump (ESP) model design

This standard ESP design assumes clean, single-phase oil production, minimal free gas removed by a gas separator, low-viscosity fluid, and a constant-frequency AC power supply. These conditions allow the use of a simple and straightforward ESP design method.[47] The ESP was designed following the methodology proposed by [105]. Only the key design parameters and final results are presented here, while the detailed design procedure can be found in the referenced work.

3. Case study

3.1. Basic information of the case study

A base case on Well AG-119X in Egypt's Abu El Gharadig Field, Western Desert, is examine to illustrate the potential for downhole geothermal power generation in a multistage hydraulically fractured vertical well. It has a geothermal gradient of 4.8 °C per 328 ft. The well was drill to a total depth of 20060ft the surface temperature is 20 °C, while the reservoir temperature reaches 171 °C. The well was cased to the bottom hole with 7″, 20 lb./ft. API casing, followed by cementing and perforation. It was divided into ten stages, each of which was successfully hydraulically fractured.

In the design, tubing and thermoelectric generators (TEGs) are install in the first three fractured stages near the heel. Specifically, 3.5 in, 9.3 lb./ft., with a 2 $\frac{1}{16}$ in inner pipe is placed inside to a depth of 12598 ft. A series of 500ft-long TEGs are attached to the outer surface of the tubing (Figure 18) The tubing is insulated with a material having a thermal conductivity of 0.068 W/(m·K). The well construction details, along with reservoir and fluid properties used in the analysis, are summarize in Table 4. For the base case, equal production.

Table 3. Integrated System Assumptions

Category	Parameter	Value	Justification/Source
TEG	Thermoelectric Material	Bi_2Te_3	Ref. [107]
TEG	ZT	0.99	Literature data
TEG	Maximum Efficiency	8.9 %	Calculated
Inverter	SiC MOSFET Efficiency	97 %	Literature
Inverter	Switching Frequency	15 kHz	Design assumption
Electrical System	Cable Efficiency	97 %	Assumed
ESP	Motor Efficiency	90–95 %	Manufacturer data
ESP	Operating Frequency	60 Hz	Design basis
Well Conditions	Reservoir Temperature	171°C	Field data
Well Conditions	Production Rate	5000 bpd	Case study data

Table 4. Parameters of the vertical well and target formation in this case study

	P-type N-type	P-type N-type
Thermoelectric Material	Bi2 − xSbxTe3	Bi2Se3 − yTey
Seebeck coefficient	222.48	− 223.06
Electrical Resistivity,	12.5	12.9
Thermal Conductivity,	1.36	1.41
Length,	0.013	0.013
Cross-section Area,	0.5	0.5

Table 5. Thermoelectric properties of the TEG material in this case study

Parameters	Value	Unit
Injection Pipe OD	2.063	in
Injection Pipe ID	1.751	in
Bottomhole Depth	20000	ft
Circulation Depth	19000	ft
Reservoir Temperature	171	°C
Cold Fluid Injection Temperature	30	°C
Production Rate	5000	bbl/d
Cold Fluid Injection Rate	1500	bbl/d
Water Specific Heat Capacity	4.187	kJ/ (kg K)
Formation Thermal Conductivity	2.42	W/(mK)
Cold Fluid Injection Rate	120	m^(3)/d

Table 6. Parameters used in ESP design in this case study

Well physical data	
Casing OD	7 in
Tubing ID	2 1/16in
Tubing OD	3.5 in
Tubing new	Yes
Perforation interval	(19500-20000) ft
Pump depth	19000 ft
Casing ID	6.01 in
Well performance data	
WHP @ desired rate	300 psi
CHP @ desired rate	20 psi
Desired liquid rate	5000 bbl/d
Water cut	0%
SBHP	8000 psi
PI	2 bpd/psi
GOR produced	50 scf/bbl
Pump suction temp.	250˚F
WHP @ desired rate	300 psi
Fluid properties	
Sp.Gr. of oil	0.85
Sp.Gr. of water	1.0
Sp.Gr. of gas	0.6
Sp.Gr. of oil	0.85
Sp.Gr. of water	1.0

4. Results

4.1. Model Validation

Validated against published experimental and numerical data using the Bi2Te3 material properties listed in Table 7 the mathematical model computes the tubing and annulus temperature distributions presented in (Figure 19). As highlighted by the gray circles in (Figure 19), converting heat into electricity within the TEG-equipped sections (the first 500 ft of each of the three stages) cause's three distinct thermal shifts: a decrease in produced fluid temperature accompanied by a corresponding temperature rise in the injected fluid.

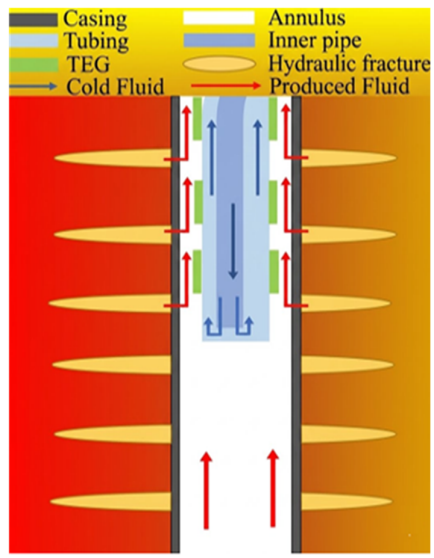

Figure 15. Wellbore construction for downhole power generation in the case study

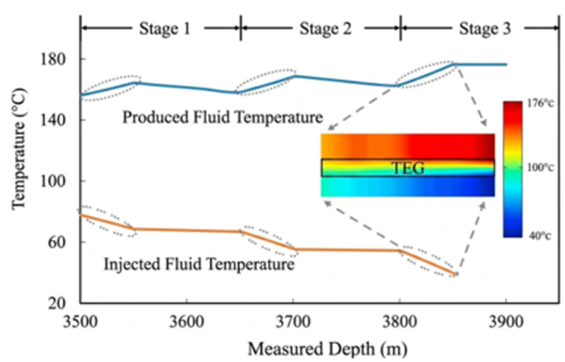

Figure 16. Temperature of produced fluid and injected fluid in three stages

Table 7. Validation Literature

Study	Efficiency
Present	8.9
Literature	8.5
Error	4.7%

Table 8.Thermoelectric performance in this case study.

Thermoelectric Parameters	Value	Unit
Figure of Merit (Z)	0.00583	K^{-1}
Dimensionless Figure of Merit (ZT)	0.99	/
Optimal Efficiency	8.9%	/
Maximum Power Output	340,059	W

As illustrated in (Figure 18), fluid temperature profiles along the wellbore split into two distinct recurring segments: TEG-equipped sections (highlighted by gray circles) and intermediate thermal recovery sections[110]. Within the TEG sections, heat conduction and Joule heating slightly raise the injected fluid's temperature, though thermal insulation keeps this increase minimal. Meanwhile, the produced fluid cools during energy conversion but is continuously restored and reheated by upstream fluid inflows before entering the next stage[110].

In this study, a dimensionless figure of merit (ZT) of 0.99 is obtained, and the maximum thermal-to-electric conversion efficiency is calculated to be 8.9%, corresponding to a peak power output of 340,059 W. The thermoelectric performance metrics are summarized in Table 5.

To further assess TEG performance, the results are compared with both experimental and numerical studies reported in the literature that employ the same thermoelectric material. Key comparison parameters, including the dimensionless figure of merit and power generation efficiency, are presented in Table 6 demonstrating that the proposed system exhibits highly competitive thermoelectric performance.

Table 9. Thermoelectric Performance Comparison with other results from the literature

Study	Downhole TEG	PowerElectronics	ESP Integration	Complete Well Design	Temp Range	Power
Wang et al. [4]	✓	✗	✗	✗	30–180°C	280 kW
Liu et al. [39]	✓	✗	✗	✗	40–176°C	310 kW
Ding et al. [40]	✓	✗	✗	✗		
Qiao et al. [42]	✓	✗	✗	✗		
Present Study	✓	✓ SiC Inverter	✓	✓	30–171°C	340 kW

4.2. Inverter design

This section examines the selection of the DC-link capacitor type and its voltage rating. Initially, the minimum capacitance required to limit the maximum voltage ripple is analyzed. Afterward, the computed capacitance values are verified against the RMS ripple current requirements[111].

The minimum capacitance capable of sustaining the maximum allowable voltage ripple is defined in Equation 33. The parameter $|C\Delta V|_{\max}$ represents the highest value of the vector [$|C\Delta V_4|_{\max}$, maximum of the 3D plot]. Equation 33, $V_{\text{ripple},\max}$ denotes the permissible peak ripple voltage, which is set to ±2.5% of the DC-link voltage V_DC. For a 600 V DC-link, this corresponds to a ripple voltage of 30 V[112].

For the three-phase SynRM presented in Equation 32, the motor peak current is 17.3 A. Under these conditions, the value of $|C\Delta V_4|_{\max}$ is calculated as 7.2083×10^{-5}, while the maximum value obtained from the 3D plot is 7.2076×10^{-5}. Therefore, $|C\Delta V|_{\max}$ is taken as 7.2083×10^{-5}. Based on Equation 34, the minimum capacitance required to maintain the voltage ripple within ±2.5% of the DC-link voltage is 4.8 μF. However, this value is not final, as the selected capacitor must also be capable of handling the DC-link current ripple.

$$C_{min} = \frac{2*|C\Delta V|_{max}}{V_{ripple,max}}, \quad (49)$$

$$C_{\min} = \frac{2*7.2083*10^{-5}}{30} = 4.8\mu F \quad (50)$$

The voltage rating of a capacitor should always be at least twice, or at a minimum 1.5 times,[113]. the maximum voltage that could occur in the circuit. For a 600 V DC-link, a capacitor rated at 900 V with a capacitance of 4.8 μF is initially selected. Three main types of DC-link capacitors are commonly used in electric drive applications: multilayer ceramic capacitors, metallized polypropylene film capacitors, and aluminum electrolytic capacitors. [114,115].

4.3. For ESP design

4.4. Electrical Power Flow and System Efficiency Analysis

The DC power generated by the thermoelectric generators cannot be deliver directly to the ESP motor; it must first pass through a SiC-based inverter, a step-up transformer, and an electrical transmission system. Consequently, conversion and transmission losses reduce the net power available to operate the ESP below the gross power generated, defining the overall electrical efficiency of the integrated system:

$$\eta_{overall} = \eta_{inv} \times \eta_{cable} \times \eta_{trans} \quad (51)$$

where η_{inv} is the inverter efficiency, and η_{cable} represents the cable efficiency

Table 10. ESP design Results in this case study

ESP design Results.	
$\boldsymbol{FBHP}$	5500 psi
$\boldsymbol{L_{dyn}}$	19000 ft
$\boldsymbol{\Delta H_{fr}}$	855 ft
Pd	815 ft
$\boldsymbol{TDH}$	5725
Stages	128 stages
$\boldsymbol{BHP}_{pump}$	128 stages. 3.5 HP/stage .85 SG; 400 HP or 450 HP Motor system required
Component	Specification for 5000 bpd @19000 ft
Pump type	High–capacity centrifugal

5.4.1. Electrical transmission efficiency.

The net power delivered to the ESP motor is calculated as:

$$Coverage\ Ratio = \frac{Pnet}{PTEG} * 100 \quad (52)$$

$$P_{net} = P_{TEG} \times \eta_{inv} \times \eta_{cable} \times \eta_{trans} \quad (53)$$

For the present case study:

P_{TEG} =340.059 KW

η_{inv} = 97%

η_{trans}=98%

η_{cable} = 97%

Therefore,

P_{net} = 340.059 × 0.97 × 0.97 ×.98

P_{net} = 313.8 kW

The results show that approximately 92.3% of the generated thermoelectric power is retained following electrical conversion and transmission losses. This net available power covers a substantial portion of the ESP energy demand, confirming the technical feasibility of the integrated system under the evaluated operating conditions.

Table 11. Electrical Power Flow Through the Integrated System

Parameter	Value
TEG Gross Power	340.1 kW
Inverter Efficiency	97 %
Transformer Efficiency	98 %
Cable Efficiency	97 %
Overall Electrical Efficiency	92.3 %
Net Power to ESP	313.8 kW

Comparing the net electrical power of the integrated TEG–SiC–ESP system with ESP demand confirms the technical feasibility of the concept. After accounting for conversion and transmission losses, the system delivers approximately 313.8 kW exceeding the ~298 kW requirement of a 400 HP ESP motor. With a coverage ratio of roughly 105%, the harvested geothermal power is theoretically sufficient to fully run the ESP.

For a 450 HP ESP motor requiring approximately 336 kW, the integrated system achieves a coverage ratio of roughly 93%, demonstrating its capacity to meet the vast majority of operational power demand. Unlike previous studies that focused solely on estimating geothermal generation potential, this work establishes a direct power-matching relationship between generated electrical energy and actual ESP requirements, validating a unified framework that combines thermoelectric generation, power conditioning, and ESP operation.

5. Sensitivity study

To enhance and optimize downhole power generation, the key design parameters influencing system performance are identified, and the effects of these parameters are systematically evaluated.

5.1. Production rate

Produced fluid movement is critical in downhole power generation design, functioning as the heat source for the TEG's hot side while supplying thermal energy to produced fluids from preceding

stages[116]. Because production rate fluctuations directly alter hot-side temperatures and electrical output, this study investigated both total and stage-specific production rates to assess their thermal and power impacts, with the corresponding produced (solid lines) and injected (dashed lines) fluid temperature profiles illustrated in(Figure 20).

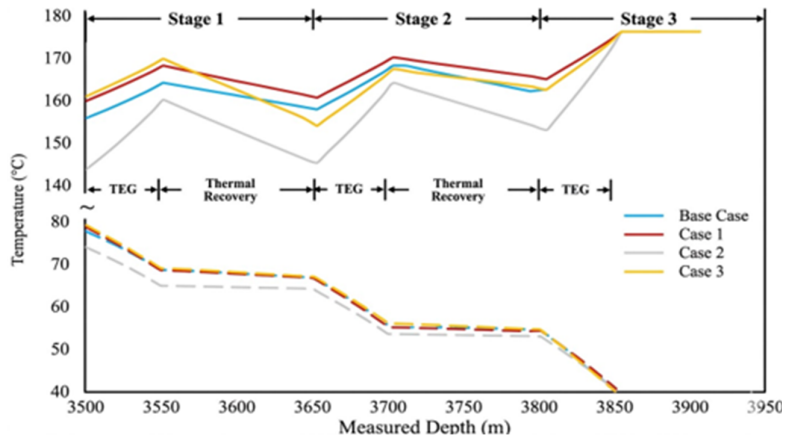

Figure 17. Temperature profiles for different production rate cases

A comparison of Case 1 and Case 2 with the base case shows that at higher production rates, corresponding to higher flow velocities, the produced fluids pass through the TEG more rapidly. This reduces the time available for heat transfer from the produced fluid through the TEG to the injected fluid[117], leading to less heat extraction for power generation, a smaller temperature decreases in the produced fluid, and a smaller temperature rise in the injected fluid. In contrast, lower production rates allow longer residence time.[118,119].

5.2. Injection rate

The injection rate is another critical parameter influencing power generation performance, as it plays a key role in sustaining a low temperature on the cold side of the TEG. Likewise, variations in the injection rate affect the overall temperature distribution.[120].

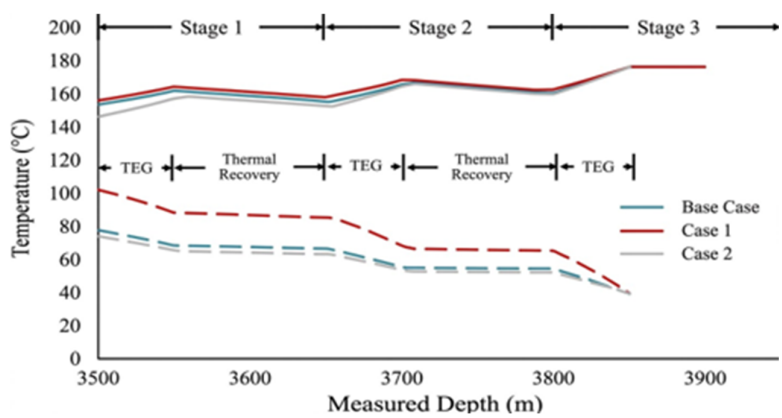

Figure 18. Temperature profiles for different injection rate cases.

Impact of the injection rate is examined by adjusting it from 80 m³/day (Case 1) to 240 m³/day (Case 2), with the corresponding results presented in (Figure 21) The temperature profiles clearly show that a higher cold-fluid injection rate, as in Case 2, more effectively cools the cold side of the TEG, resulting in the lowest cold-side temperature.[121] In contrast, changes in the cold-fluid injection rate have minimal influence on the hot-side temperature, which is primarily controlled by the produced fluids. Consequently, increasing the cold-fluid injection rate is beneficial for maintaining a low temperature on the cold side of the TEG[122].

5.3. Effect of Geothermal Gradient

To evaluate the influence of subsurface thermal conditions on the performance of the proposed system, a sensitivity analysis was conduct by varying

the geothermal gradient while maintaining all other operating and design parameters constant. The geothermal gradient is one of the most influential factors affecting the temperature difference across the thermoelectric modules and, consequently, the amount of electrical power generated. Table 12 summarizes the predicted thermoelectric power output for different geothermal gradient values representative of various reservoir conditions.

Table 12. Effect of Geothermal Gradient on Thermoelectric Power Generation

Geothermal Gradient (°C/100m)	Generated Power (kW)
3.5	210
4.0	270
4.8	340
5.5	410
6.0	470

The results indicate a strong positive correlation between geothermal gradient and generated electrical power. As the geothermal gradient increases from 3.5 to 6.0 °C/100 m, the predicted power output increases from 210 kW to 470 kW. This trend is attributed to the larger temperature difference available across the thermoelectric modules, which enhances heat transfer and improves thermoelectric conversion performance.

To investigate the impact of thermoelectric generator (TEG) installation length on system performance, a sensitivity analysis was perform by varying the total active TEG length while maintaining identical reservoir and operating conditions. The installation length directly influences the available heat-transfer area and the number of thermoelectric modules participating in energy conversion. Therefore, increasing the TEG length is expected to enhance the total electrical power generation capacity of the proposed system. Table 13 presents the predicted electrical power output

Table 13. Sensitivity of Thermoelectric Power Generation to TEG Installation Length

TEG Length (m)	Generated Power (kW)
50	120
100	230
150	340
200	430

System performance scales significantly with TEG installation length, as extending the active length from 50 m to 200 m increases generated electrical power from 120 kW to 430 kW due to the expanded heat-exchange surface area and higher module count. As indicated in Table 14, optimizing installation length is critical to meeting ESP operational power demand. Under the evaluated conditions, the selected base-case length of 150 m yields approximately 340 kW of electrical power, striking a practical balance between power generation capability and physical installation requirements.

Table 14. Effect of Thermoelectric Figure of Merit (ZT) on Conversion Efficiency

ZT	Efficiency
0.8	6.5%
0.9	7.8%
1.0	8.9%
1.2	10.5%

Sensitivity analysis reveals a strong positive relationship between the thermoelectric figure of merit ZT and system efficiency, with predicted conversion efficiency rising from 6.5% to 10.5% as ZT increases from 0.8 to 1.2. This performance gain occurs because high ZT materials convert thermal energy into electrical energy more effectively while minimizing conductive heat losses. Consequently, material selection is critical to downhole power generation, and future advancements in thermoelectric materials will be essential to boosting the power capacity and overall feasibility of geothermal-assisted ESP systems.

5.4. Uncertainty Analysis

To evaluate the robustness of the proposed model, an uncertainty analysis was conducted considering variations in the most influential input parameters, including geothermal gradient (±10%), thermoelectric material figure of merit ZT (±10%), thermal conductivity (±10%), and production rate (±10%).

The results indicate that the predicted electrical power output varies between 295 kW and 382 kW around the base-case value of 340 kW. The geothermal gradient was identified as the dominant uncertainty source.

5.5. Practical and Economic Limitations

Although the simulation results demonstrate promising technical feasibility, several practical challenges remain before field deployment can be achieve. The present study does not consider long-term degradation of thermoelectric materials under high-temperature and high-pressure downhole environments. In addition, installation complexity, maintenance requirements, electrical insulation reliability, and mechanical integrity of the TEG modules require further investigation. This study did not evaluate economic feasibility or capital costs, and

its single-case findings may not generalize to wells with differing geothermal gradients or reservoir conditions.

6. Discussion and Conclusions

6.1. Discussion

Compared with conventional geothermal binary-cycle systems and ORC-based geothermal recovery technologies, the proposed TEG-ESP architecture eliminates turbines, working fluids, and large surface facilities. Furthermore, it utilizes existing well infrastructure and enables localized downhole power generation close to the electrical load (ESP motor), potentially reducing transmission losses and installation complexity This study presents a simulation-based framework for evaluating the feasibility of downhole geothermal power generation integrated with ESP systems.

6.1.1. Thermal Behavior and Temperature Gradient Optimization.

The two-dimensional wellbore heat transfer model demonstrates that the vertical configuration provides a sustained high-temperature environment along substantial well depth. By circulating cold fluid inside the tubing while hot produced fluids flow in the annulus, a stable and enhanced temperature gradient is established across the TEG modules. The introduction of effective thermal conductivity simplifies thermoelectric coupling without sacrificing modeling accuracy. The results indicate that:

- Power output scales strongly with temperature differential.
- Formation thermal conductivity and injection flow rate significantly influence steady-state
- Joule heating effects slightly reduce net gradient but can be compensated through optimized module placement.

Compared to surface-based geothermal TEG systems, the downhole configuration reduces surface heat losses and utilizes existing infrastructure, improving overall thermodynamic utilization.

6.1.2. Inverter Performance and SiC Device Advantages

The use of SiC MOSFETs in the three-phase VSI substantially enhances switching performance compared to conventional silicon IGBTs. Analytical and waveform-based loss calculations show:

- Lower switching and conduction losses.
- Higher allowable switching frequencies.
- Improved efficiency at elevated temperatures.

The SVPWM-based ripple analysis reveals that DC-link voltage ripple is strongly dependent on modulation index and power factor. The maximum RMS ripple current does not occur at unity power factor under realistic operating conditions, emphasizing the importance of selecting capacitance based on maximum output power rather than theoretical worst-case unity-PF assumptions. Proper DC-link capacitor sizing:

- Prevents excessive thermal stress.
- Reduces EMI.
- Maintains voltage stability for ESP motor operation.

6.1.3. Integration with ESP Systems

The integration of thermoelectric generation with ESP systems provides a novel hybrid energy-production configuration. The ESP design section confirms:

- Accurate TDH calculation is essential for stage selection.
- Pump efficiency and BEP alignment significantly affect overall system power demand.
- Frictional losses must be limited (<10% of total energy demand) for economic feasibility.

6.2. Conclusions

This study presents a comprehensive and integrated framework for downhole geothermal power generation in vertical oil wells using thermoelectric generators coupled with SiC-based inverter technology and optimized ESP system design. A two-dimensional heat transfer model was developed to accurately predict temperature distribution within the wellbore, incorporating thermoelectric conversion effects through an effective thermal conductivity formulation.

The results demonstrate that:

1- Vertical well configurations enable sustained and significant temperature gradients suitable for thermoelectric energy conversion.

2- SiC-based voltage source inverters offer superior efficiency and reduced switching losses compared to conventional silicon-based systems.

3- Analytical DC-link ripple modeling enables precise capacitor sizing under realistic operating conditions.

4- Integration with ESP design demonstrates compatibility with artificial lift requirements

The proposed hydrocarbon–geothermal co-production transforms produced thermal energy, previously treated as a byproduct, into a valuable distributed energy resource.

(Figure 19) shows the overall architecture of the proposed system. Thermal energy extracted from Future work should focus on experimental validation at the field scale, long-term reliability analysis of downhole TEG modules, economic assessment under varying oil price scenarios, and optimization of thermoelectric material performance. The integration of geothermal recovery with oil production represents a potentially promising transitional pathway toward cleaner and more efficient energy systems within the petroleum industry.

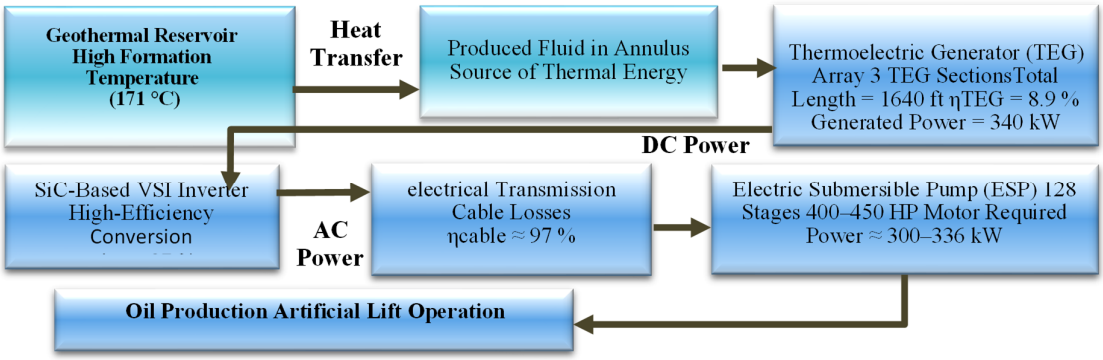

Figure 19. Integrated TEG–SiC–ESP System Architecture

References

[1]. Ben Cheikh, R., El Badsi, B., & Masmoudi, A. (2021). Geothermal sources-based thermoelectric power generation: An attempt to enhance the rural electrification in southern Tunisia. *Energies*, *14*(3), Article 746.

[2]. Alimonti, C., & Soldo, E. (2016). Study of geothermal power generation from a very deep oil well with a wellbore heat exchanger. *Renewable Energy*, *86*, 292–301.

[3]. Chen, J., Li, K., Liu, C., Li, M., Lv, Y., Jia, L., & Gao, F. (2017). Enhanced efficiency of thermoelectric generator by optimizing mechanical and electrical structures. *Energies*, *10*(9), Article 1329.

[4]. Wang, K., Liu, J., & Wu, X. (2018). Downhole geothermal power generation in oil and gas wells. *Geothermics*, 76, 141–148.

[5]. Wang, K., Yuan, B., Ji, G., & Wu, X. (2018). A comprehensive review of geothermal energy extraction and utilization in oilfields. *Journal of Petroleum Science and Engineering*, 168, 465–477.

[6]. Ahiska, R., & Mamur, H. (2014). A review: thermoelectric generators in renewable energy. *International Journal of Renewable Energy Research*, 4(1), 128–136.

[7]. Kadu, A., Patil, T., & Somatkar, S. (2026). Thermoelectric Generator for Waste Heat Recovery System. *International Research Journal of Innovation in Science and Technology*, 1(1), 52-58.

[8]. Snyder, G. J., & Toberer, E. S. (2008). Complex thermoelectric materials. *Nature Materials*, 7(2), 105–114.

[9]. Wang, K., & Wu, X. (2019). Downhole thermoelectric generation in unconventional horizontal wells. *Fuel*, 254, 115530.

[10]. Wang, K., & Wu, X. (2019). Transient thermoelectric generation in oil wells under transient production. *Proceedings of the 44th Stanford Geothermal Workshop*.

[11]. Li, K. A kind of underground heat exchange power generation pipeline and underground power generation system.

[12]. Zhu, Y. *Numerical simulation study on enhancing the efficiency of thermoelectric power generation*. China University of Geosciences.

[13]. Zare, V., & Palideh, V. (2018). Employing thermoelectric generator for power generation enhancement in a Kalina cycle driven by low-grade geothermal energy. *Applied Thermal Engineering*, 130, 418–428.

[14]. Baranowski, L. L., Snyder, G. J., & Toberer, E. S. (2012). Effective thermal conductivity in thermoelectric materials. *Journal of Applied Physics*, 111(12), 124904.

[15]. Wang, K., Wu, X., & Liu, J. (2017). Downhole geothermal power generation in oil and gas wells. *GRC Transactions*, 41.

[16]. Li, K., et al. (2020). An expandable thermoelectric power generator and the experimental studies on power output. *International Journal of Heat and Mass Transfer*, 160, 120205.

[17]. Zayed, M. E., Shboul, B., Yin, H., Zhao, J., & Zayed, A. A. (2023). Recent advances in geothermal energy reservoirs modeling: Challenges and potential of thermo-fluid integrated models for reservoir heat extraction and geothermal energy piles design. *Journal of Energy Storage*, 62, 106835.

[18]. Legg, L. V. Simple plan for high-WOR wells improves efficiency. *Oil & Gas Journal*, 127–131.

[19]. Xie, H., et al. (2023). Design and performance of a modular 1 kilowatt-level thermoelectric generator for

geothermal application at medium-low temperature. *Energy Conversion and Management*, 298, 117782.

[20]. Wang, K., Yuan, B., Ji, G., & Wu, X. (2018). A comprehensive review of geothermal energy extraction and utilization in oilfields. *Journal of Petroleum Science and Engineering*, 168, 465–477.

[21]. Zhang, H., Li, K., Zhu, Y., & Jia, L. (2023). Numerical study on the performance of the thermoelectric generator with different air-water mixtures. *Geothermics*, 107, 102601.

[22]. Eisenhut, C., & Bitschi, A. TE conversion system based on Geothermal and Solar Heat. *Conference on Thermoelectrics*.

[23]. Xia, E., et al. (2024). Optimal design of a high-performance heat exchanger for modular thermoelectric generator towards low-grade thermal energy recovery. *Applied Thermal Engineering*, 258, 124849.

[24]. Mohammadi, Z., & Fallah, M. (2023). Conventional and advanced exergy investigation of a double flash cycle integrated by absorption cooling, ORC, and TEG power system driven by geothermal energy. *Energy*, 282, 128372.

[25]. Wang, L., et al. (2025). Coaxial geothermal wellbore thermoelectric power generation system: design, experimentation, and performance analysis. *Applied Thermal Engineering*, 271, 126349.

[26]. Mahmoudan, A., Esmaeilion, F., Hoseinzadeh, S., Soltani, M., Ahmadi, P., & Rosen, M. (2022). A geothermal and solar-based multigeneration system integrated with a TEG unit: Development, 3E analyses, and multi-objective optimization. *Applied Energy*, 308, 118399.

[27]. Reinhardt, T., Johnson, L. A., Popovich, N., & Poplar, N. (2011). Systems for electrical power from coproduced and low temperature geothermal resources. *Proceedings of 36th Workshop on Geothermal Reservoir Engineering*.

[28]. Liu, J., Wang, Z., Shi, K., Li, Y., Liu, L., & Wu, X. (2020). Analysis and modeling of thermoelectric power generation in oil wells: A potential power supply for downhole instruments using in-situ geothermal energy. *Renewable Energy*, 150, 561–569.

[29]. Yang, S., Chen, H., & Luo, D. (2025). A comprehensive review of thermoelectric generators from micropower supply to kilowatt system. *Green Energy and Fuel Research*, 2(2), 93-108.

[30]. Lan, Y., Lu, J., & Wang, S. (2024). An experimental study on the performance of TEGs using uniform flow distribution heat exchanger for low-grade thermal energy recovery. *Energy*, 292, 130506.

[31]. Lou, Y., Liu, G., Romagnoli, A., & Ji, D. (2023). TEG-ORC combined cycle for geothermal source with coaxial casing well. *Applied Thermal Engineering*, 226, 120223.

[32]. Liao, J., et al. (2023). Effect of operating conditions on the output performance of a compact TEG for low-grade geothermal energy utilization. *Applied Thermal Engineering*, 236, 121878.

[33]. Xie, H., et al. A novel in-situ power generator system for geothermal resources without fluid extraction. *ARMA US Rock Mechanics/Geomechanics Symposium*.

[34]. Abdalgader, I. A. S., Kivrak, S., & Özer, T. (2022). Power performance comparison of SiC-IGBT and Si-IGBT switches in a three-phase inverter for aircraft applications. *Micromachines*, 13(2), 313.

[35]. Sinha, A., & Joshi, Y. K. (2012). Downhole electronics cooling using a thermoelectric device and heat exchanger arrangement. *Journal of Electronic Packaging*, 134(1).

[36]. Gou, X., Yang, S., Xiao, H., & Ou, Q. (2013). A dynamic model for thermoelectric generator applied in waste heat recovery. *Energy*, 52, 201–209.

[37]. Chen, J., Wang, R., Ding, R., Liu, W., Jiang, Y., & Luo, D. (2025). Innovative design and numerical optimization of a cylindrical thermoelectric generator for vehicle waste heat recovery. *Energy Conversion and Management*, 326, 119478.

[38]. Cheng, F., Hong, Y., Zhang, B., & Tang, W. (2017). Experimental optimization of the area-specific power for thermoelectric modules. *Spacecraft Environment Engineering*, 34(3), 329–334.

[39]. Khan, Z. H., et al. Optimized thermoelectric generation for efficient low-medium temperature geothermal energy harvesting. *Renewable Energy*, 122032.

[40]. Li, K., et al. (2021). Field test of thermoelectric generators at Bottle Rock Geothermal Power Plant. *Journal of Power Sources*, 485, 229272.

[41]. Wang, W., Shahvali, M., & Su, Y. (2015). A semi-analytical fractal model for production from tight oil reservoirs with hydraulically fractured horizontal wells. *Fuel*, 158, 612–618.

[42]. Li, K., Bian, H., Liu, C., Zhang, D., & Yang, Y. (2015). Comparison of geothermal with solar and wind power generation systems. *Renewable and Sustainable Energy Reviews*, 42, 1464–1474.

[43]. Meng, M., Qiu, Z., Zhong, R., Liu, Z., Liu, Y., & Chen, P. (2019). Adsorption characteristics of supercritical CO2/CH4 on different types of coal and a machine learning approach. *Chemical Engineering Journal*, 368, 847–864.

[44]. Khan, M. I., Franke, L., Rösch, A. G., Wang, Z., Mallick, M. M., Alegría, P., & Lemmer, U. (2026). Thermoelectric generators for harvesting medium-temperature geothermal anomalies: printed vs bulk devices. *Applied Thermal Engineering*, 130125.

[45]. Xin, S., Liang, H., Hu, B., & Li, K. (2012). A 400 kW geothermal power generator using co-produced fluids from Huabei oilfield. *GRC Transactions*, 36, 1173–1176.

[46]. S. P. Handbook. *No Title*. Claremore, Oklahoma.

[47]. Nolen, K. B., & Gibbs, S. G. How to match submersible pumps to well performance. *World Oil*, 41–45.

[48]. Pankratz, R. E., & Wilson, B. L. (1988). Predicting power cost and its role in ESP economics. *SPE Rocky Mountain Regional Meeting*, Casper, WY.

[49]. Vandevier, J. E. (1987). Optimum power cable sizing for electric submersible pumps. *SPE Production Operations Symposium*, Oklahoma City, OK.

[50]. French, S. W. (1991). Optimum cable selection of electrical submersible pumps. *SPE Production Operations Symposium*, Oklahoma City, OK.

[51]. Tijunelis, D., & Wargin, R. (1977). Cable selection process for submersible oil well pumps. *Proceedings of the 24th Southwestern Petroleum Short Course*, Lubbock, TX, 181–185.

[52]. Liang, B., Meng, X., Miao, Z., & Li, X. (2026). Performance enhancement of thermoelectric modules through the introduction of macro-porous thermoelectric leg. *Energy*, 139942.

[53]. Legg, L. V. Correct electrical components boost production from high-WOR wells. *Oil & Gas Journal*, 60–63.

[54]. Sau, S., & Fernandes, B. G. (2019). Modular multilevel converter based variable speed drive with reduced capacitor ripple voltage. *IEEE Transactions on Industrial Electronics*, 66(5), 3412–3421.

[55]. Trochimiuk, P., Kopacz, R., Frac, K., & Rabkowski, J. (2022). Medium voltage power switch in silicon carbide—A comparative study. *IEEE Access*, 10, 26849–26858.

[56]. Wong-Loya, J. A., Santoyo, E., & Andaverde, J. (2017). A 3-D wellbore simulator (WELLTHERSIM) to determine the thermal diffusivity of rock-formations. *Computers & Geosciences*, 103, 204–214.

[57]. Tawfiq, K. B., Ibrahim, M. N., El-Kholy, E. E., & Sergeant, P. (2021). Comparative analysis of refurbishing methods of three-phase synchronous reluctance machines to five-phase with minimum cost. *IEEE Transactions on Industry Applications*, 57(6), 6007–6022.

[58]. Xu, Y., Fang, C., Cui, B., Ji, G., Zhai, Y., & Liu, D. (2011). Gated electronic currents modulation and designs of logic gates with single molecular field effect transistors. *Applied Physics Letters*, 99(1), 013109.

[59]. Ahmed, M. R., Todd, R., & Forsyth, A. J. (2019). Predicting SiC MOSFET behavior under hard-switching, soft-switching, and false turn-on conditions. *IEEE Transactions on Power Electronics*, 34(9), 9001–9011.

[60]. Vujacic, M., Dordevic, O., & Grandi, G. (2020). Evaluation of DC-link voltage switching ripple in multiphase PWM voltage source inverters. *IEEE Transactions on Power Electronics*, 35(4), 3478–3490.

[61]. Yang, Y., Wen, Y., & Gao, Y. (2019). A novel active gate driver for improving switching performance of high-power SiC MOSFET modules. *IEEE Transactions on Power Electronics*, 34(8), 7775–7787.

[62]. Wang, H., & Blaabjerg, F. (2014). Reliability of capacitors for DC-link applications in power electronic converters—An overview. *IEEE Transactions on Industry Applications*, 50(5), 3569–3578.

[63]. Ji, G., Li, D., Fang, C., Xu, Y., Zhai, Y., & Cui, B. (2012). Effect of contact interface configuration on electronic transport in (C20)2-based molecular junctions. *Physics Letters A*, 376(6-7), 773–778.

[64]. Ahiska, R., & Mamur, H. (2016). Development and application of a new power analysis system for testing of geothermal thermoelectric generators. *International Journal of Green Energy*, 13(7), 672–681.

[65]. Tanaka, T., Wang, H., & Blaabjerg, F. (2019). A DC-link capacitor voltage ripple reduction method for a modular multilevel cascade converter with single delta bridge cells. *IEEE Transactions on Industry Applications*, 55(6), 6115–6126.

[66]. Lea, J. F., Turpin, J. L., & Bearden, J. L. (1986). Correlation of performance data for electric submersible pumps with gas-liquid flow. *Proceedings of the 33rd Southwestern Petroleum Short Course*, Lubbock, TX, 267–281.

[67]. Standing, M. B. (1947). A pressure-volume-temperature correlation for mixtures of California oils and gases. *API Drilling and Production Practice*, 275–286.

[68]. Zhang, D., Wang, F., Burgos, R., Lai, R., & Boroyevich, D. (2011). DC-link ripple current reduction for paralleled three-phase voltage-source converters with interleaving. *IEEE Transactions on Power Electronics*, 26(6), 1741–1753.

[69]. Tawfiq, K. B., Ibrahim, M. N., El-Kholy, E. E., & Sergeant, P. (2022). Construction of synchronous reluctance machines with combined star-pentagon configuration using standard three-phase stator frames. *IEEE Transactions on Industrial Electronics*, 69(8), 7582–7595.

[70]. Yuan, B., Su, Y., Moghanloo, R. G., Rui, Z., Wang, W., & Shang, Y. (2015). A new analytical multi-linear solution for gas flow toward fractured horizontal wells with different fracture intensity. *Journal of Natural Gas Science and Engineering*, 23, 227–238.

[71]. Torres, R. A., Dai, H., Jahns, T. M., & Sarlioglu, B. (2019). Operation and analysis of current-source inverters using dual-gate four-quadrant wide-bandgap power switches. *IEEE Energy Conversion Congress and Exposition (ECCE)*, Baltimore, MD, USA, 2353–2360.

[72]. Ji, G., Cui, B., Xu, Y., Fang, C., Zhao, W., & Li, D. (2014). Enhanced rectifying performance by asymmetrical gate voltage for BDC20 molecular devices. *RSC Advances*, 4(32), 16537–16542.

[73]. Mocevic, S., et al. Design of a 10 kV SiC MOSFET-based high-density high-efficiency modular medium-voltage power converter.

[74]. Zhao, T., Wang, J., Huang, A. Q., Agarwal, A., & IGBT, S. Based motor drive systems. *Proceedings of the IEEE Industry Applications Annual Meeting*, New Orleans, LA, USA, 331–335.

[75]. Guo, J., Ye, J., & Emadi, A. (2018). DC-link current and voltage ripple analysis considering antiparallel diode reverse recovery in voltage source inverters. *IEEE Transactions on Power Electronics*, 33(6), 5171–5180.

[76]. Tawfiq, K. B., Mansour, A. S., & Sergeant, P. (2023). Mathematical design and analysis of three-phase inverters: Different wide bandgap semiconductor technologies and DC-link capacitor selection. *Mathematics*, 11(9), 2137.

[77]. Yu, X., Tsai, C. Y., Chu, Y. W., Chueh, C. C., & Li, Z. A. (2025). Regioisomeric Control of Charge Transport

Properties in Fluoranthene-Fused 12-Ring Heteroarenes. *JACS Au*, 5(7), 3483-3490.

[78]. Taha, W., Azer, P., Poorfakhraei, A., Dhale, S., & Emadi, A. (2022). Comprehensive analysis and evaluation of DC-link voltage and current ripples in symmetric and asymmetric two-level six-phase voltage source inverters. *IEEE Transactions on Power Electronics*, 37(2), 2215–2229.

[79]. Li, W., et al. (2023). Performance skutterudite/half-Heusler cascaded thermoelectric module using the transient liquid phase sintering joining technique. *ACS Applied Materials & Interfaces*, 15(2), 2961–2970.

[80]. Ji, D., Liu, G., Romagnoli, A., Rajoo, S., Besagni, G., & Markides, C. N. (2024). Low-grade thermal energy utilization: Technologies and applications. *Applied Thermal Engineering*, 244, 122618.

[81]. Meng, M., Baldino, S., Miska, S. Z., & Takach, N. (2019). Wellbore stability in naturally fractured formations featuring dual-porosity/single-permeability and finite radial fluid discharge. *Journal of Petroleum Science and Engineering*, 174, 790–803.

[82]. Cheng, W. L., Liu, J., Nian, Y. L., & Wang, C. L. (2016). Enhancing geothermal power generation from abandoned oil wells with thermal reservoirs. *Energy*, 109, 537–545.

[83]. Wu, K., & Wang, X. (2019). Transient thermoelectric generation in oil wells under transient production. *Proceedings of the 44th Stanford Geothermal Workshop*.

[84]. Zhu, Y., Li, K., Linghu, J., Yuan, P., Zuo, S., & Weng, Z. (2024). Modeling study on the geometric optimization of thermoelectric modules. *Journal of Energy Resources Technology*, 146(1).

[85]. Wang, K., & Wu, X. (2018). A design of downhole thermoelectric generation for horizontal oil wells. *GRC Transactions*, 42.

[86]. Zhang, Y., et al. (2023). Defect-engineering-stabilized AgSbTe2 with high thermoelectric performance. *Advanced Materials*, 35(11), 2208994.

[87]. Liu, X., Falcone, G., & Alimonti, C. (2018). A systematic study of harnessing low-temperature geothermal energy from oil and gas reservoirs. *Energy*, 142, 346–355.

[88]. Lee, W., & Lee, J. (2018). Development of a compact thermoelectric generator consisting of printed circuit heat exchangers. *Energy Conversion and Management*, 171, 1302–1310.

[89]. Zhao, Y., Yan, X., Fan, Y., Ge, M., Yue, L., & Wang, S. (2021). Analysis of optimal humidification temperature for a flue gas thermoelectric generation system with gas humidification. *Journal of Cleaner Production*, 285, 125467.

[90]. Santos, V. D., Cougo, B., Roux, N., Sareni, B., Revol, B., & Carayon, J. (2014). Trade-off between losses and EMI issues in three-phase SiC inverters for aircraft applications. *IEEE International Symposium on Electromagnetic Compatibility*, Washington, DC, USA, 55–60.

[91]. Mannen, T., & Fujita, H. (2016). A DC capacitor voltage control method for active power filters using modified reference including the theoretically derived voltage ripple. *IEEE Transactions on Industry Applications*, 52(5), 4179–4187.

[92]. Safayet, A., Islam, M. S., & Sebastian, T. (2022). Comprehensive analysis for DC-link capacitor sizing for a three-phase current controlled voltage source inverter. *IEEE Transactions on Industry Applications*, 58(4), 4248–4260.

[93]. Fuentes, C. D., Müller, M., Bernet, S., & Kouro, S. (2021). SiC-MOSFET or Si-IGBT: Comparison of design and key characteristics of a 690 V grid-tied industrial two-level voltage source converter. *Energies*, 14(11), 3054.

[94]. Zhao, W., Ji, G., & Liu, D. (2014). Contact position and width effect of graphene electrode on the electronic transport properties of dehydrobenzoannulenne molecule under bias. *Physics Letters A*, 378(5-6), 446–452.

[95]. Pei, X., Zhou, W., & Kang, Y. (2015). Analysis and calculation of DC-link current and voltage ripples for three-phase inverter with unbalanced load. *IEEE Transactions on Power Electronics*, 30(10), 5401–5412.

[96]. Powers, M. L. (1986). Economic considerations for sizing tubing and power cable for electric submersible pumps. *SPE Annual Technical Conference and Exhibition*, New Orleans, LA.

[97]. Takacs, G. (2017). *Electrical submersible pumps manual: Design, operations, and maintenance*. Gulf Professional Publishing.

[98]. Gosnold, W. Electric power generation from low to intermediate temperature resources executive.

[99]. Visan, A. I., Negut, I., & Hapenciuc, C. (2025). Recent Advances in Thermoelectric Materials for Biomedical Applications: Energy Harvesting and Wearables.

[100]. Vujacic, M., Dordevic, O., Mandrioli, R., & Grandi, G. (2022). DC-link low-frequency current and voltage ripple analysis in multiphase voltage source inverters with unbalanced load. *IET Electric Power Applications*, 16(3), 300–314.

[101]. Cui, B., Xu, Y., Ji, G., Wang, H., Zhao, W., & Zhai, Y. (2014). A single-molecule diode with significant rectification and negative differential resistance behavior. *Organic Electronics*, 15(2), 484–490.

[102]. El-Hadary, M. I., Senthilraja, S., & Zayed, M. E. (2023). A hybrid system coupling spiral type solar photovoltaic thermal collector and electrocatalytic hydrogen production cell: Experimental investigation and numerical modeling. *Process Safety and Environmental Protection*, 170, 1101–1120.

[103]. Koseki, K., Yonezawa, Y., Mizushima, T., Matsunaga, S., Iizuka, Y., & Yamaguchi, H. (2018). Dynamic behavior of a medium-voltage N-channel SiC-IGBT with ultrafast switching performance of 300 kV/μs. *IEEE Transactions on Industry Applications*, 54(4), 3558–3565.

[104]. Wang, L., Xu, J., Chen, Q., Chen, Z., Geng, X., & Lin, K. (2022). Improved PWM strategies to mitigate dead-time distortion in three-phase voltage source converter. *IEEE Transactions on Power Electronics*, 37(12), 14692–14705.

[105]. Han, D., Li, S., Wu, Y., Choi, W., & Sarlioglu, B. (2019). Comparative analysis on conducted CM EMI

emission of motor drives: WBG versus Si devices. *IEEE Transactions on Power Electronics*, 34(9), 8353–8363.

[106]. Wang, K., & Wu, X. (2019). Transient thermoelectric generation in oil wells under transient production. *Proceedings of the 44th Stanford Geothermal Workshop*.

[107]. Kumar, S., Heister, S. D., Xu, X., Salvador, M., Jr., & P, G. (2013). Thermoelectric generators for automotive waste heat recovery systems part I: Numerical modeling and baseline model analysis. *Journal of Electronic Materials*, 42(4), 665–674.

[108]. Wang, K., & Wu, X. (2019). Downhole thermoelectric generation in unconventional horizontal wells. *Fuel*, 254, 115530.

[109]. Wang, K., Liu, J., & Wu, X. (2018). Downhole geothermal power generation in oil and gas wells. *Geothermics*, 76, 141–148.

[110]. Sasaki, K., Horikawa, D., & Goto, K. (2015). Consideration of thermoelectric power generation by using hot spring thermal energy or industrial waste heat. *Journal of Electronic Materials*, 44(1), 391–398.

[111]. Oswald, N., Anthony, P., McNeill, N., & Stark, B. H. (2014). An experimental investigation of the tradeoff between switching losses and EMI generation with hard-switched all-Si, Si-SiC, and all-SiC device combinations. *IEEE Transactions on Power Electronics*, 29(5), 2393–2407.

[112]. Perdikakis, W., Scott, M., Yost, K. J., Kitzmiller, C., Hall, B., & Sheets, K. A. (2020). Comparison of Si and SiC EMI and efficiency in a two-level aerospace motor drive application. *IEEE Transactions on Transportation Electrification*, 6(4), 1401–1411.

[113]. Yang, F., et al. (2023). Compact-interleaved packaging method of power module with dynamic characterization of 4H-SiC MOSFET and development of power electronic converter at extremely high junction temperature. *IEEE Transactions on Power Electronics*, 38(1), 417–434.

[114]. Fouejio, D., Noudem, P., Tefouet, I. F., Nyandou, P. B., & Zekeng, S. S. (2026). DFT investigations of electro-optical and charge transport properties of two photochromic isomers 3, 6-bis-((E)-2-(benzo [b] thiophen-5 (6)-yl) vinyl) phenanthrene (BTVP) for OLED and NLO applications. *Discover Applied Sciences*.

[115]. Li, S., Yang, L., & Wang, T. (2022). Analysis of the DC-link voltage ripple for the three-phase voltage source converter under nonlinear output current. *Energies*, 15(8), 2892.

[116]. Qiao, Y., Shi, K., & Liu, J. (2024). Analytical study of integrating downhole thermoelectric power generation with a coaxial borehole heat exchanger in geothermal wells. *Scientific Reports*, 14(1), 505.

[117]. Liu, C., Chen, P., & Li, K. (2014). A 500 W low-temperature thermoelectric generator: Design and experimental study. *International Journal of Hydrogen Energy*, 39(27), 15497–15505.

[118]. Xie, J., Tonkin, R., Yeh, A., Wang, J., & O'Sullivan, M. (2025). Application of a geothermal wellbore simulator in evaluating an enhanced geothermal system. *Geothermics*, 125, 103160.

[119]. Zhu, Y., et al. (2021). Power generation at low temperatures using thermoelectric generators and cost analysis. *International Journal of Energy Research*, 2021, 8728700.

[120]. Lund, J. W., & Toth, A. N. (2021). Direct utilization of geothermal energy 2020 worldwide review. *Geothermics*, 90, 101915.

[121]. Gholamian, E., Habibollahzade, A., & Zare, V. (2018). Development and multi-objective optimization of geothermal-based organic Rankine cycle integrated with thermoelectric generator and proton exchange membrane electrolyzer for power and hydrogen production. *Energy Conversion and Management*, 174, 112–125.

[122]. Li, G., Yang, M., Meng, Y., Wen, Z., Wang, Y., & Yuan, Z. (2016). Transient heat transfer models of wellbore and formation systems during the drilling process under well kick conditions in the bottom-hole. *Applied Thermal Engineering*, 93, 339–347.

انجمن مهندسی معدن ایران
نشریه مهندسی معدن و محیط زیست
نشانی نشریه: www.jme.shahroodut.ac.ir
دانشگاه صنعتی شاهرود

تلفیق سیستم تولید برق ترموالکتریک درون‌چاهی با اینورتر مبتنی بر کاربید سیلیکون (SiC) در طرحی نوآورانه برای راهبری پمپ‌های درون‌چاهی الکتریکی (ESP) بدون نیاز به کابل

محمد یحیی عامر[1*]، سعید کامل سالم[2] و ابراهیم صلاح‌الدین محمد[2]

۱. شرکت حفاری مصر (EDC)، مصر
۲. دانشکده مهندسی نفت و معدن، دانشگاه سوئز، مصر

اطلاعات مقاله

تاریخ ارسال: ۲۰۲۶/۰۲/۲۳
تاریخ داوری: ۲۰۲۶/۰۶/۱۴
تاریخ پذیرش: ۲۰۲۶/۰۸/۲۱

DOI: 10.22044/jme.2026.17537.3488

کلمات کلیدی

چاه‌های منابع زمین‌گرمایی در میدان‌های نفتی
فناوری ترموالکتریک
اینورتر الکتریکی پمپ‌های درون‌چاهی (ESP)
پمپ درون‌چاهی (ESP) بدون کابل

چکیده

پمپ‌های الکتریکی شناور (ESP) از جمله پرکاربردترین سیستم‌های فرازآوری مصنوعی در صنعت نفت هستند. با این حال، عملکرد آنها به شدت به توان الکتریکی تأمین‌شده از سطح زمین که از طریق کابل‌های طولانی درون چاهی منتقل می‌شود، وابسته است که منجر به تلفات قابل توجه انرژی، هزینه‌های بالای نصب، چالش‌های قابلیت اطمینان و افزایش شدت کربن می‌شود. همزمان، مقادیر زیادی از انرژی زمین‌گرمایی با وجود گرادیان‌های حرارتی قابل توجهی که به طور طبیعی در امتداد چاه موجود است، در چاه‌های هیدروکربنی عمیق بلااستفاده باقی می‌ماند. این مطالعه یک چارچوب چند رشته‌ای جدید را معرفی می‌کند که با اتصال بازیابی گرمای زمین‌گرمایی، تولید انرژی ترموالکتریک، الکترونیک قدرت پیشرفته و فناوری ESP، خود چاه را به یک سیستم تولید انرژی یکپارچه تبدیل می‌کند. برخلاف رویکردهای مرسوم که انرژی زمین‌گرمایی و فرازآوری مصنوعی را به عنوان حوزه‌های جداگانه در نظر می‌گیرند، مفهوم پیشنهادی یک معماری واحد ایجاد می‌کند که انرژی حرارتی تلف‌شده را به توان الکتریکی قابل استفاده برای عملکرد ESP تبدیل می‌کند و مسیر جدیدی را به سمت سیستم‌های فرازآوری مصنوعی مستقل از انرژی و با کابل کاهش‌یافته ایجاد می‌کند. چارچوب پیشنهادی، یک مدل انتقال حرارت دوبعدی چاه، تبدیل انرژی ترموالکتریک و بهینه‌سازی توان مبتنی بر سیلیکون-کاربید را با یک روش‌شناسی کامل طراحی ESP شامل تحلیل عملکرد جریان ورودی، تعیین هد دینامیکی کل، انتخاب پمپ و بهینه‌سازی مرحله ترکیب می‌کند. یک مطالعه موردی روی چاه AG-119X در میدان ابوالغرادیق، صحرای غربی، مصر، با عمق تنظیم پمپ ۱۹۰۰۰ فوت، امکان‌سنجی فنی تولید همزمان هیدروکربن-زمین‌گرمایی را نشان می‌دهد و پتانسیل تولید ترموالکتریک تقریباً ۳۵۰ کیلووات را در شرایط بهینه پیش‌بینی می‌کند. این مطالعه فراتر از نشان دادن بازیابی انرژی، یک نقشه راه مقیاس‌پذیر برای ادغام مستقیم منابع زمین‌گرمایی در زیرساخت‌های بالابر مصنوعی، کاهش وابستگی به منبع تغذیه خارجی، بهبود راندمان کلی سیستم و امکان‌پذیر کردن تولید نفت پایدارتر ایجاد می‌کند. رویکرد پیشنهادی گامی به سوی همگرایی مهندسی نفت، انرژی زمین‌گرمایی، علم ترموالکتریک و الکترونیک قدرت است و پایه‌ای برای سیستم‌های ESP خود-توان نسل بعدی فراهم می‌کند.

نویسنده مسئول مکاتبات: mohammed.haam@pme.suezuni.edu.eg (م. ی. عامر)